Journal of Hazardous Materials 414 (2021) 125293

Contents lists available at ScienceDirect

Journal of Hazardous Materials

journal homepage: www.elsevier.com/locate/jhazmat

Investigation of the inhibited biotoxicity of heavy metals towards 5-formylcytosine in rice by hydrochar based on photoelectrochemical biosensor

Qian Wang [a,1], Huanshun Yin [a,1], Yunlei Zhou [a], Jun Wang [b,*], Shiyun Ai [a]

[a] College of Chemistry and Material Science, Food Safety Analysis and Test Engineering Technology Research Center of Shandong Province, Shandong Agricultural University, Taian 271018, PR China

[b] College of Resources and Environment, Key Laboratory of Agricultural Environment in Universities of Shandong, Shandong Agricultural University, Taian 271018, PR China

ARTICLE INFO

Editor: Dr. Rinklebe Jörg

Keywords:
$Ag_2S@WS_2$
Photoelectrochemistry
Epigenetic modification
$FeVO_4$ artificial mimic enzyme
Ecotoxicological effects

ABSTRACT

A photoelectrochemical (PEC) biosensor was constructed for 5-formylcytosine (5fC) nucleotide detection based on $Ag_2S@WS_2$ photoactive material and $FeVO_4$ catalytic signal quenching. After $Ag_2S@WS_2$ was modified onto the ITO substrate surface, 5fC recognition reagent of Au@4-amino3hydrazino5mercapto-1,2,4-triazol (Au@AHMT) was further modified through electrostatic adsorption. Afterwards, based on the specific chemical reaction between $-NH_2$ and –CHO, 5fC can be selectively recognized and captured. Subsequently, the nanoenzyme of $FeVO_4$ was recognized based on the specific reaction between the phosphate group of 5fC nucleotide and Fe^{3+}. Under the catalysis of $FeVO_4$, the 4-chloro-1-naphthol in the detection solution can be oxidized to generate a precipitate, which will be retained on the electrode surface to inhibit the PEC signal. The developed method presented a widely dynamic range from 0.1 to 400 nM. The detection limit was 0.062 nM (3σ). This method also showed good detection selectivity, reproducibility and stability. The applicability was verified by investigating 5fC content change in genomic DNA of rice tissues after incubated with heavy metals. Moreover, the inhibited influence of hydrochar towards heavy metals was also assessed.

1. Introduction

5-Formylcytosine (5fC) is an important epigenetic modification, which is produced by 5-methylcytosine (5mC) oxidation under the catalysis of ten-eleven translocation protein. As a kind of important active DNA demethylation style, 5fC plays a pivotal role in various biological processes, including cell differentiation (Pfaffeneder et al., 2011b), gene regulation (Lopez et al., 2017), etc. Thus, the research interest has been widely aroused to reveal the role of 5fC in modulating the structure and function of genomic DNA (Wang et al., 2013a). To fully achieve this aim, monitoring 5fC level with high sensitivity and specificity is crucial. However, owing to the low abundance in genomic DNA and the structural similarity to 5mC, 5hmC and 5caC, the detection method should be precise, specific and sensitive (Liu et al., 2017). To this end, many methods for 5fC detection have been explored, including polymerase chain reaction (PCR), gene sequencing, and gene chip technique. Though these methods can achieve 5fC detection, there are problems such as complicated operation and high cost.

Breakthrough techniques have been constructed for 5fC detection, including a mass spectrometry-based method and fluorescence assay. For example, Carell's group used liquid chromatography-mass spectrometry technique to detect 5fC in genomic DNA of mouse embryonic stem cells after enzyme digestion (Pfaffeneder et al., 2011a). To achieve the specific recognition of 5fC, a biotin probe containing a hydroxylamine group was designed, which could specifically bind with aldehyde group of 5fC. In addition, a fluorescence method was investigated for 5fC detection based on the synthesized hydroxylamine fluorescent compounds, which was specifically react with 5fC (Guo et al., 2013). Although these methods can achieve the selective detection of 5fC, there are still some shortcomings, such as expensive and bulk instrument, complicated operation, difficulty in synthesizing specific recognition molecule, etc. Thus, it is still challenging for exploring new detection

* Corresponding author.
E-mail address: jwang@sdau.edu.cn (J. Wang).
[1] These two authors contributed equal to this work.

https://doi.org/10.1016/j.jhazmat.2021.125293
Received 25 September 2020; Received in revised form 30 October 2020; Accepted 19 November 2020
Available online 18 February 2021

technique for 5fC.

To solve these questions, photoelectrochemical (PEC) technique attracts our attentions. PEC is an emerging detection method for complex systems, where light is employed as the excitation source, and photocurrent is used as the output detection signal (Zhou et al., 2020). Due to the complete separation of input and output signals, the ultra-low background signal is achieved (Hao et al., 2018). Based on the advantages of inexpensive apparatus, simple operation, high sensitivity, sample volume microscale, and instrument miniaturization, PEC technique is effective tool for bioanalysis, including small molecule, nucleic acid, protein, bacteria, and cells, especially for epigenetic modification molecule (Zhou et al., 2020; Zhao et al., 2018; Li et al., 2020b, 2017, 2019, 2020a; Wang et al., 2018b, 2018b, 2019; Cai et al., 2018; Cao et al., 2018; Hao et al., 2017; Yuan et al., 2020; You et al., 2020; Xu et al., 2020). Therefore, PEC technique should also be an alternative platform for 5fC with potential application prospects.

For PEC biosensor construction, the photoactive material is crucial factor, which can greatly influence the detection sensitivity. Transition metal disulfides (TMDs) have attracted widespread interests due to the two-dimensional layered structure, excellent catalysis activity, large specific surface area (Chhowalla et al., 2013). Among various TMDs, WS_2 has attracted increasing attention for its inexpensive price, visible light activity and acceptable electron mobility, which has been applied to many fields, such as sensing and biosensing, solar cells, light-emitting diodes and photosensitive devices, especially in the field of photocatalysis (Pumera and Loo, 2014; Tan et al., 2017). WS_2 possesses sizable bandgap around 1–3 eV and displays advantageous optoelectronic properties with visible light excitation (Wilson and Yoffe, 1969). However, owing to the high recombination of photogenerated electrons-hole pairs, the application of individual WS_2 in PEC field is limited. To solve this problem, constructing heterojunction structure with other semiconductors is promising strategy, such as TiO_2/WS_2 (Ren et al., 2018), CdS QDs/WS_2 (Wei et al., 2018) and CdS/WS_2-MoS_2 (Reddy et al., 2017). Ag_2S has received widespread attention for its excellent photocatalytic performance. Considering the band gap relationship, Ag_2S can be assembled on the surface of WS_2 to form heterojunction structure. The tight combination of Ag_2S and WS_2 will inherit the excellent photocatalytic performance of Ag_2S and the excellent photoconversion performance of WS_2, which will improve the photoactivity by decreasing the transfer of carriers to the transient electron-hole pairs recombination (Lin et al., 2019).

Based on the formation of insoluble products on electrode surface, biocatalytic precipitation (BCP) is an effective signal suppression model to expand the detection limit by mass amplification in the analysis field (Patolsky et al., 2003; Zhang et al., 2019, 2018). Combining BCP with PEC technology, the detection sensitivity can be significantly improved. Thus, BCP technique has been widely used in PEC assay by forming insulating layer to change electron transport characteristics of the interface, which greatly affects the optoelectronic signal (Zhao et al., 2012). Although BCP is a widely used technology, it still suffers from the disadvantages of expensive enzyme and the influence of enzymatic activity by various extreme environments (Muche and Göbel, 1996). To solve these problems, artificial enzymes attract our attentions. $FeVO_4$ is a typical artificial mimetic enzyme with high peroxide activity that mimics the catalytic performance of horseradish peroxidase (HRP) to catalyze H_2O_2-mediated oxidation reaction (Yu et al., 2016). Compared with natural enzymes, $FeVO_4$ owns the merits of inexpensive price, simple storage conditions, easy to maintain catalytic activity, and small differences between batches.

Inspiring by the above researches, a novel PEC assay was developed for 5fC detection based on $Ag_2S@WS_2$ heterojunction and $FeVO_4$ nanoenzyme. To assess the applicability, the influence of two kinds of heavy metals (Cd^{2+} and Hg^{2+}) on the expression of 5fC in genomic DNA of rice seedlings tissues was investigated. Moreover, the influence of hydrochar on the toxicity of heavy metals to 5fC expression was also investigated.

2. Experimental section

See Supporting Information.

3. Results and discussion

3.1. Detection strategy

A novel and simple PEC biosensor was constructed for 5fC detection. Since 5fC exists in DNA as nucleotide, 5-formyl-2'-deoxycytidine-5'-triphosphate was employed as target molecule, which was abbreviated as 5fdCTP. As presented in Scheme 1, $Ag_2S@WS_2$ was adopted as photoactive substance, where Ag_2S greatly improved the photoactivity of WS_2 owing to the formation of heterojunction. After the modification of $Ag_2S@WS_2$ on ITO electrode, 4-amino3hydrazino5mercapto-1,2,4-triazol (AHMT) functionalized gold nanoparticles (AuNPs, this AuNP-based nanomaterial was abbreviated as Au@AHMT) was further modified based on electrostatic adsorption, where AHMT was employed as 5fdCTP recognition and capture reagent and AuNPs were employed as electron transfer accelerator and AHMT carrier for capturing more 5fdCTP. Actually, 5fdCTP was recognized and captured by means of the covalent reaction between $–NH_2$ of AHMT and –CHO of 5fC. Finally, $FeVO_4$ was captured through the complexation between the phosphate group of 5fdCTP and Fe^{3+} (Ahmed Ouameur et al., 2005). As a kind of artificial mimic enzyme, $FeVO_4$ can catalyze the oxidation reaction of 4-chloro-1-naphthol to produce benzo-4-chlorohexadienone in the presence of H_2O_2. Benzo-4-chlorohexadienone can be then deposited onto the electrode surface as an insulating film, which can quench the PEC response, achieving 5fdCTP detection.

3.2. Material characterization

To prove the successful synthesis of nanomaterials, they were characterized with various techniques. As seen in Fig. 1A, the bulk WS_2 (a) showed a massive structure with a length of several microns, which was further confirmed by TEM image (Fig. 1C). However, the exfoliated WS_2 nanosheets presented a small lamellar structure with a length of tens to hundreds of nanometers (Fig. 1B and D). The exfoliated WS_2 nanosheets were also investigated by UV–vis spectrum (Fig. 1E). The peaks at 624 nm and 518 nm were the characteristic absorption bands for exfoliated WS_2 in solution (Zhao et al., 2016; Yuan et al., 2014; Vega-Mayoral et al., 2016). Fig. 1F presented the AFM image of WS_2 nanosheets, which indicated 4 layers of WS_2 nanosheets because the thickness for single layer WS_2 is about 0.8 nm (Xu et al., 2015), proving the successful exfoliation of bulk WS_2.

Fig. 1G illustrated the SEM image of Ag_2S, which showed irregular nanoparticle structure. After Ag_2S was synthesized on the surface of WS_2, much small Ag_2S nanoparticles were observed (Fig. 1H). The mapping of $Ag_2S@WS_2$ (Fig. S1, see Supporting Information) showed that Ag, W, and S elements were uniformly distributed in the composite material, which further clarified the successful preparation of $Ag_2S@WS_2$ composite. The small amount of W element might be caused by the thickness layer of Ag_2S on WS_2 surface. The prepared $Ag_2S@WS_2$ was also characterized by PL, XRD and Raman. PL can reflect the rate of photo-activated electron-hole complexation. As shown in Fig. 1I, pure WS_2 nanosheets showed the strongest PL spectra with peaks at 485, 529, and 543 nm, exhibiting the strong recombination of electron-hole pairs. Upon combination with Ag_2S, the peaks of WS_2 nanosheets decreased a little, indicating that the decreased recombination of electron-hole pairs and improved photoactivity of $Ag_2S@WS_2$. To further prove the successful combination of Ag_2S and WS_2 nanosheets, the crystal structure of Ag_2S, WS_2 and $Ag_2S@WS_2$ composite nanomaterial was investigated by XRD. As illustrated in Fig. 1J, the diffraction peaks of WS_2 and Ag_2S were consistent with WS_2 (JCPDS 08-0237) and Ag_2S (JCPDS 14-0072) in standard card. WS_2 appeared peaks at 14.3°, 28.9°, 32.7°, 33.5°, 39.5°, 43.9°, 49.6°, 58.4°, and 59.9°, corresponding to planes of (002), (004),

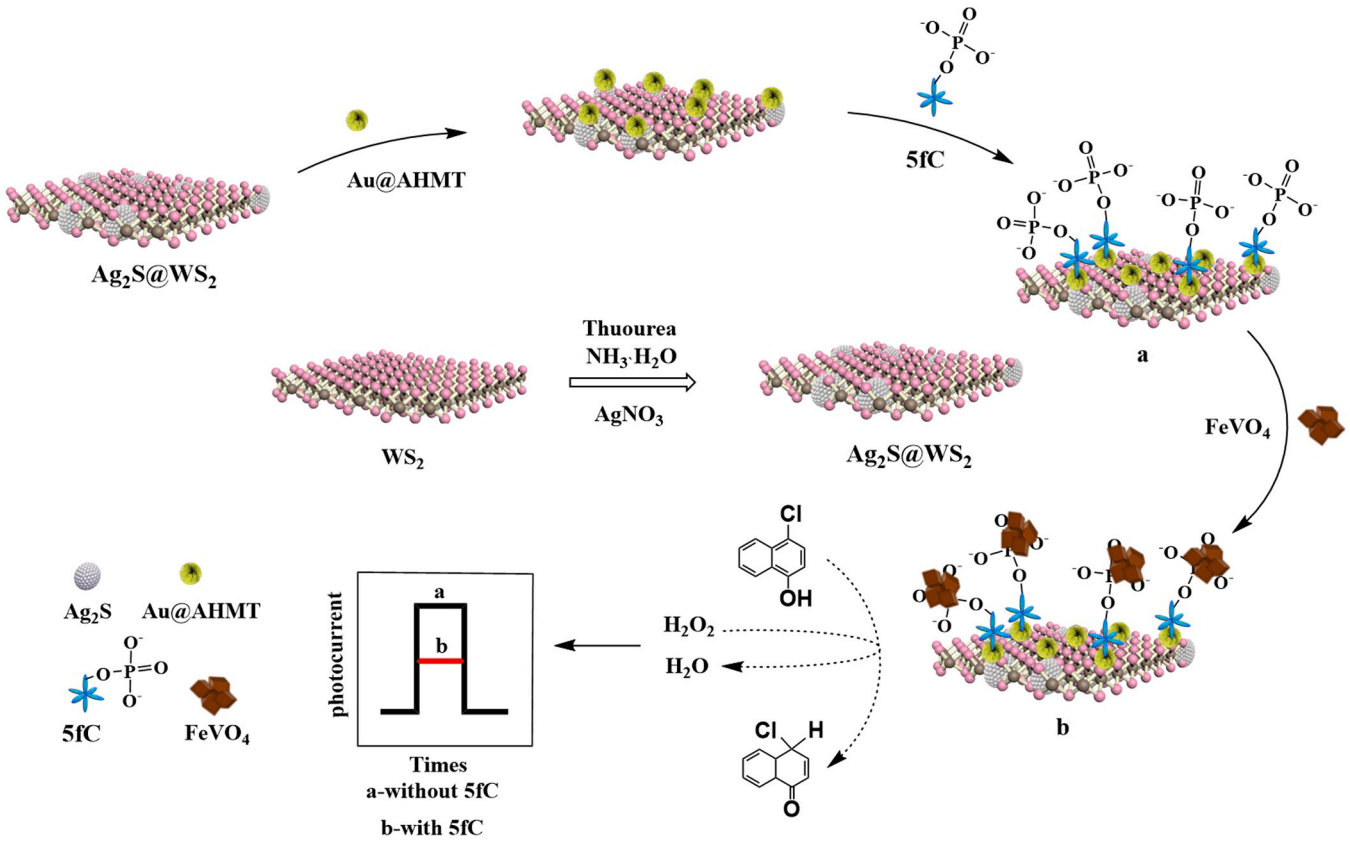

Scheme 1. Schematic illustration of the biosensor fabrication process and 5fdCTP detection.

(100), (101), (103), (006), (105), (110), (112). The peaks for Ag_2S were presented at 29.0°, 31.6°, 33.6°, 34.4°, 36.8°, 37.7°, and 40.8°, which correspond to the planes of (111), (− 112), (120), (− 121), (121), (− 103), (031), and (200) (Lin et al., 2019). These diffraction peaks appeared in the curves of $Ag_2S@WS_2$ composite nanomaterial, which proved the successful preparation of $Ag_2S@WS_2$ composite nanomaterial. Fig. 1K illustrated the Raman spectroscopy of Ag_2S, WS_2 and $Ag_2S@WS_2$. WS_2 nanosheets showed two peaks at 351.6 and 420.3 cm^{-1} (curve a), which were well-matched with $E^1{}_{2g}$ in-plane vibrations and A_{1g} vertical plane vibrations, respectively (Wang et al., 2013b). In the same region, Ag_2S presented no obvious Raman adsorption peak (curve b). After WS_2 nanosheets were combined with Ag_2S, the intensity of Raman adsorption peak decreased accompanying the slight shift (curve c), where the $E^1{}_{2g}$ was shifted from 348.4 to 350.4 cm^{-1}, and A_{1g} was shifted from 417.2 to 419.7 cm^{-1}. It might be caused by the combined Ag_2S. Based on the above characterizations, the successful preparation of $Ag_2S@WS_2$ and $FeVO_4$ can be confirmed. In addition, the morphology of hydrochar was characterized by SEM, which presented small spherical structure (Fig. 1L).

The synthesized AuNPs were evaluated by TEM technique, which presented spherical structure of AuNPs with the diameter of about 13 nm (Fig. 2A). Fig. 2B illustrated the photograph of $HAuCl_4$ solution, AuNPs dispersion and Au@AHMT dispersion with yellow, red wine and dark purple, respectively. To further prove the preparation of Au@AHMT, the mapping of Au@AHMT was performed. As seen in Fig. S2, the elements for Au, C, N, and S were observed at Au@AHMT. Because AHMT contains C, N, S and H elements, the successful preparation of Au@AHMT was confirmed.

The prepared $FeVO_4$ was characterized by SEM and XRD. $FeVO_4$ presented an irregular cube nanostructure. The average length was about 120 nm and the width was about 100 nm (Fig. 2C). Fig. 2D illustrated the XRD pattern of $FeVO_4$. The diffraction peak of $FeVO_4$ was in general agreement with the standard card (JCPDS 25-0418) and consistent with previous report (Yu et al., 2016), which indicated the successful preparation of $FeVO_4$. However, the diffraction peaks of $FeVO_4$ were weak, which indicated that the crystallinity of $FeVO_4$ was poor and the product might be in amorphous form.

In this work, $FeVO_4$ was employed as nanozyme with the activity of horseradish peroxidase (HRP). To testify this activity, a colorimetric analysis experiment was performed (Fig. 2E). Due to the absence of catalyst, the oxidation of TMB by H_2O_2 was slowly. Thus, no blue TMB oxidation product was obtained (tube a). However, when $FeVO_4$ dispersion was added into the system, the solution quickly changed from colorless to blue (tube b). It strongly proved the mimic HRP activity of $FeVO_4$. The color change was also confirmed by visible spectrum (Fig. 2F).

3.3. Mechanism investigation for photoactivity improvement

To certificate the improved photoactivity of WS_2 nanosheets by Ag_2S, the photocurrent of different electrodes was measured. As presented in Fig. 3A, the photocurrent for WS_2/ITO (curve a) and Ag_2S@ITO (curve b) was 75 and 2080 nA, respectively. When WS_2 nanosheets were combined with Ag_2S, the photocurrent was improved greatly to 4040 nA (curve c). This phenomenon is attributed to the combination of WS_2 nanosheets and Ag_2S, which increased the electron transfer rate and decreased the recombination of photogenerated electron-hole pairs. To prove the formation of heterojunction structure of $Ag_2S@WS_2$, the VB-XPS, electrochemical mott-schottky curve and UV–Vis DRS of WS_2 and Ag_2S were investigated. As illustrated in Fig. 3B and C, the slope for electrochemical mott-schottky curves of WS_2 and Ag_2S were both positive, indicating *n*-type semiconductors of WS_2 and Ag_2S. The flat band potential (E_{fb}) was calculated to be 0.17 V and 0.06 V for WS_2 and Ag_2S, respectively. The valence band (E_{vb}) can be calculated based on the equation of $E_{vb} = E_{fB} + E_{VB\text{-}XPS}$. Thus E_{vb} for WS_2 and Ag_2S was about 1.19 V and 0.92 V (vs. SCE), which was about

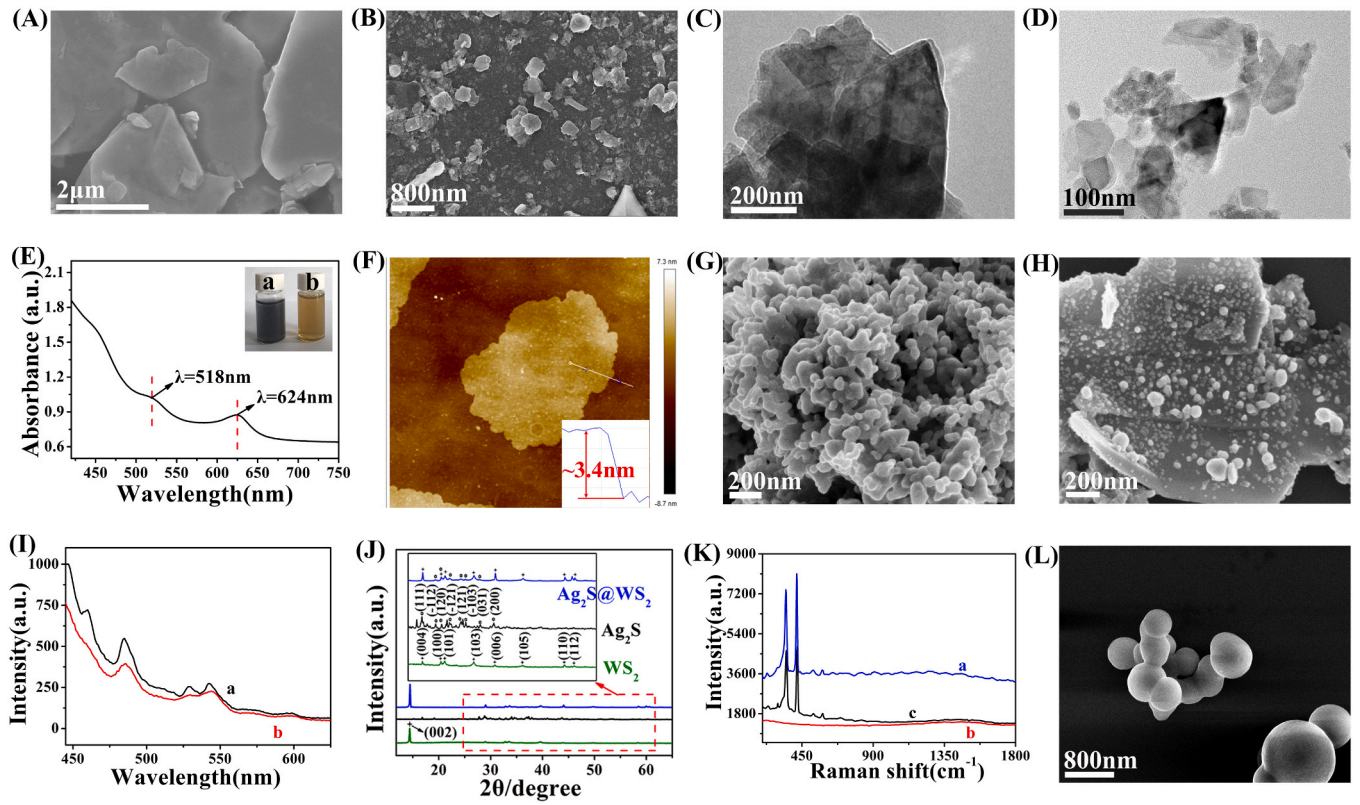

Fig. 1. SEM images of bulk WS_2 (A), WS_2 nanosheets (B), Ag_2S (G) and $Ag_2S@WS_2$ composite (H). TEM images of bulk WS_2 (C) and WS_2 nanosheets (D). (E) UV–vis absorption images of WS_2 nanosheets (inset: solution color images of bulk WS_2 (a) and WS_2 nanosheets (b)). (F) AFM image of WS_2 nanosheets. (I) PL spectra of WS_2 (a) and $Ag_2S@WS_2$ (b). (J) XRD patterns of WS_2, $Ag_2S@WS_2$ and Ag_2S. (K) Raman spectra of WS_2 nanosheets (a), Ag_2S (b) and $Ag_2S@WS_2$ (c). (L) SEM image of hydrochar. (For interpretation of the references to color in this figure legend, the reader is referred to the web version of this article.).

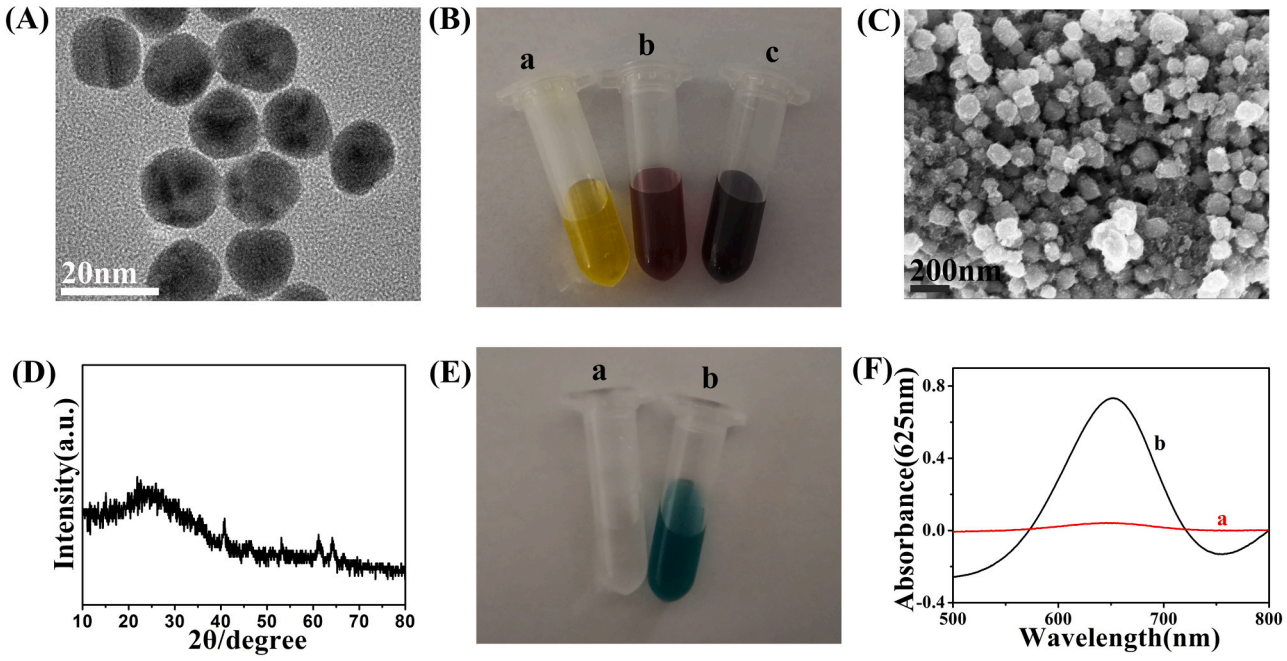

Fig. 2. (A) TEM image of AuNPs. (B) Color comparison of $HAuCl_4$, AuNPs and Au@AHMT. (C) SEM of $FeVO_4$. (D) XRD of $FeVO_4$. Color changes (E) and UV–vis absorption spectra (F) of different color reaction systems. (a) H_2O_2 + TMB, (b) H_2O_2 + TMB + $FeVO_4$. (For interpretation of the references to color in this figure legend, the reader is referred to the web version of this article.).

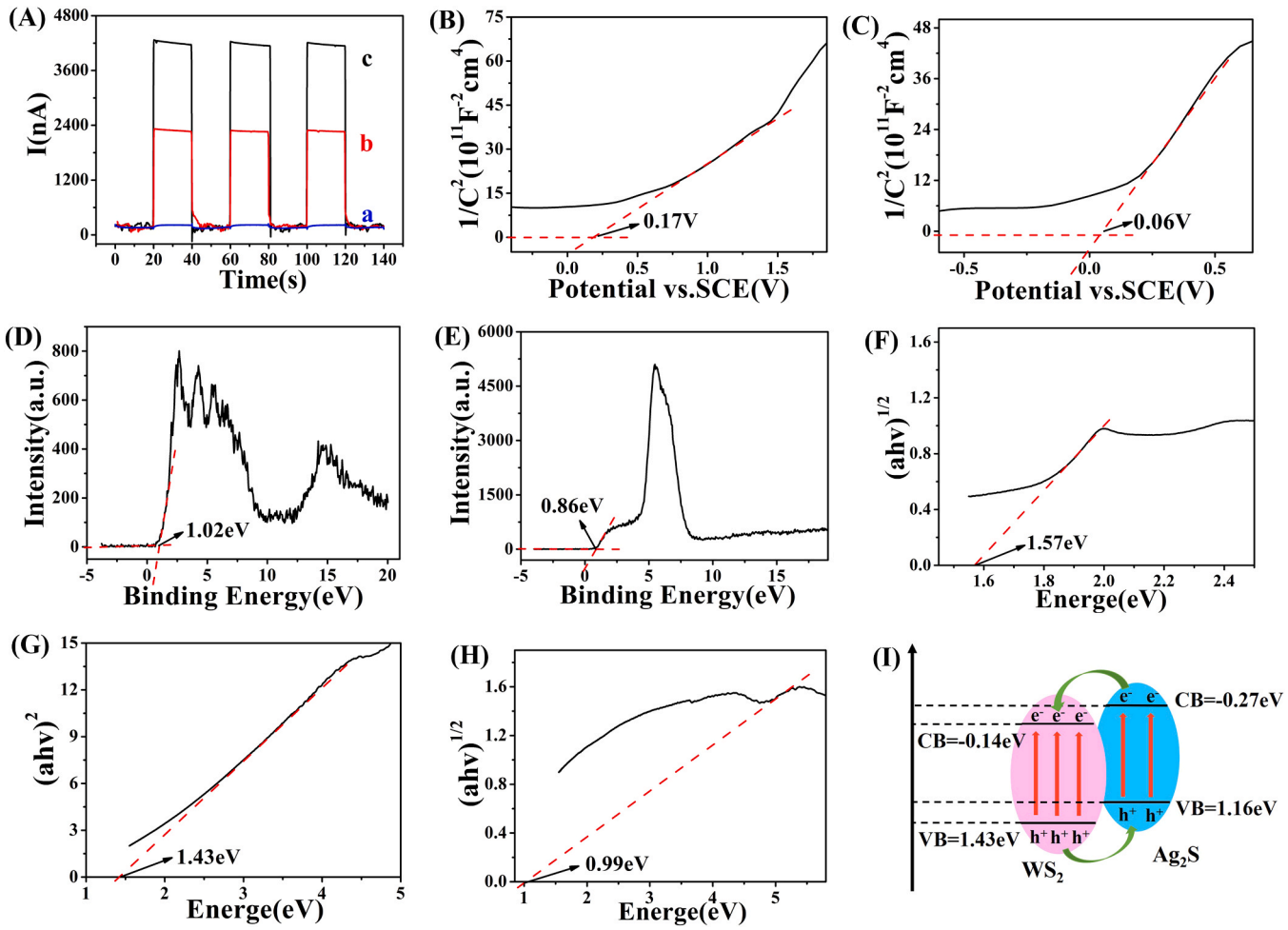

Fig. 3. (A) Photocurrent response of different electrodes under visible light irradiation. (a) WS_2/ITO, (b) Ag_2S/ITO, (c) Ag_2S@WS_2/ITO. Mott-Schottky plots of WS_2 (B) and Ag_2S (C). VB-XPS spectra of WS_2 (D) and AgS_2 (E), UV–Vis DRS of WS_2 (F), AgS_2 (G) and AgS_2/WS_2 (H). (I) Schematic illustration of the matched energy bands of WS_2 and Ag_2S.

0.24 V smaller than the value vs. NHE. Thus E_{vb} for WS_2 and Ag_2S was about 1.43 V and 1.16 V (vs. NHE) for WS_2 and Ag_2S (Fig. 3D and E), respectively (Lin et al., 2019; Di et al., 2019; Zang et al., 2018). The bandgap energies (E_g) for WS_2 and Ag_2S were about 1.57 eV and 1.43 eV according to the UV–Vis DRS as illustrated in Fig. 3F and G. Therefore, the conduction band (E_{cb}) was calculated to be as − 0.14 eV (WS_2) and − 0.27 (Ag_2S) eV according to the equation of $E_{vb} = E_{cb} + E_g$. Based on these data, a schematic illustration of band structure for WS_2 and Ag_2S was drawn as shown in Fig. 3I, which confirmed the formation of WS_2/Ag_2S heterojunction structure. The matched energy band improved the electron transfer rate, which decreased the recombination of photogenerated electron-hole pairs, and improved the photoactivity. To further confirm the improved photoactivity, the bandgap energy for the composite of Ag_2S@WS_2 was also investigated using UV–Vis DRS as shown in Fig. 3H, and the results indicated the bandgap energy of 0.99 eV, which was lower than that of WS_2 (1.57 eV) and Ag_2S (1.43 eV). The narrow bandgap energy can promote the transfer rate, and improve the photoactivity. Based on the above investigation, it can be concluded that the formed heterojunction structure of Ag_2S@WS_2 greatly improves the photoactivity.

3.4. Detection feasibility assay

EIS is an effective tool for monitoring electrode interface change, and evaluate the electrode fabrication process. Thus, the electrode modification process was characterized by EIS. In Nyquist plot, the diameter of the semicircle represents the interface electron transfer resistance (R_{et}). As shown in Fig. 4A, the ITO electrode showed a small semicircle (curve a), indicating small R_{et}. Then, the R_{et} decreased when Ag_2S@WS_2 was modified on ITO surface (curve b). It is attributed to the enlarged electrode area, which facilitates the diffusion of redox probe to electrode area. Moreover, the zeta potential of Ag_2S@WS_2 is positive (Fig. 4C), which is also beneficial to the diffusion of the negative redox probe. Afterwards, the R_{et} value further decreased due to the good conductibility of AuNPs (curve c), facilitating the electron migration. When 5fdCTP was specifically captured, the R_{et} of 5fC/Au@AHMT/Ag_2S@WS_2/GCE increased (curve d). The phosphate group of 5fdCTP repelled the migration of the redox probe to electrode surface due to the strong electrostatic repulsion effect. Subsequently, the R_{et} value further increased when $FeVO_4$ was captured (curve e), causing by the semiconductor property of $FeVO_4$, decreasing the electron transfer rate. According to the change of the R_{et} value, the successful preparation of the modified electrodes can be confirmed.

Fig. 4B provided the PEC response of various electrodes in PEC detection buffer. No photocurrent was observed at ITO electrode (curve a). However, after Ag_2S@WS_2 nanocomposite was modified onto the ITO electrode surface, a strong photocurrent response was obtained (curve b), indicating the good photoactivity of Ag_2S@WS_2 nanocomposite. Then, the photocurrent decreased when Au@AHMT was electrostatically adsorbed on Ag_2S@WS_2/ITO (curve c), which was caused by the energy transfer between Ag_2S@WS_2 semiconductor composite and Au@AHMT (Zhao et al., 2018; Shu et al., 2016; Shi et al.,

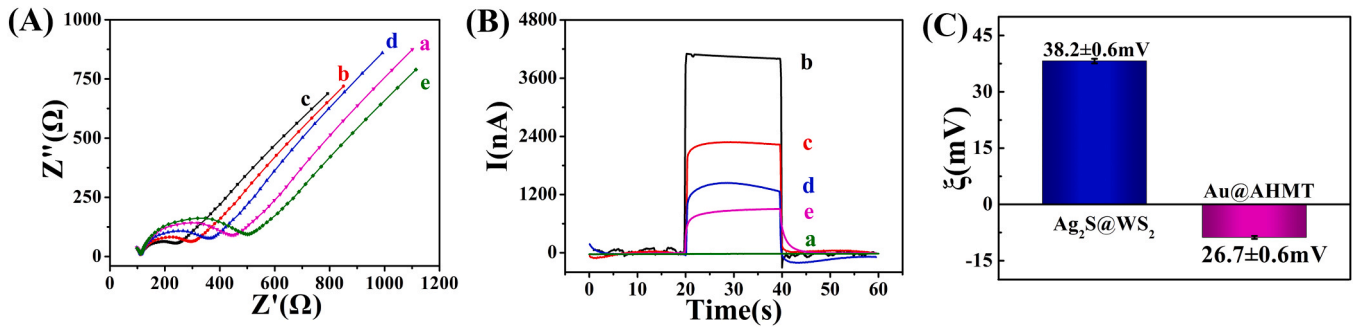

Fig. 4. (A) Nyquist plot for different electrodes in EIS detection buffer. (B) Photocurrent response of different electrodes in PEC detection buffer under visible light irradiation. For graphs A and B, (a) ITO, (b) $Ag_2S@WS_2$/ITO, (c) Au@AHMT/$Ag_2S@WS_2$/ITO, (d) 5fC/Au@AHMT/$Ag_2S@WS_2$/ITO, (e) $FeVO_4$/5fC/Au@AHMT/$Ag_2S@WS_2$/ITO. (C) Zeta potential of $Ag_2S@WS_2$ and Au@AHMT.

2018; He et al., 2018). Afterwards, the PEC response further reduced when 5fdTP was captured (curve d). It is attributed to the increased steric hindrance effect and electrostatic repulsion effect, causing by the immobilized 5fdCTP. After the modification of the artificial simulation enzyme of $FeVO_4$, the photocurrent significantly reduced (curve e). $FeVO_4$ can catalyze H_2O_2 to oxidize 4-chloro1-naphthol in the detection solution to produce benzene-4-chlorohexanedione, which will form insulation film on the electrode surface, blocking the migration of photogenerated electron, enlarging the recombination of photogenerated electro-hole pairs, and leading to a decreased photocurrent. Based on the photocurrent change, the application of this biosensor for 5fdCTP detection can be certified.

3.5. Optimization

To achieve high detection sensitivity, several parameters were optimized, including mass ratios of WS_2 and Ag_2S, $Ag_2S@WS_2$ concentration, Au@AHMT concentration, 5fdCTP incubation time, $FeVO_4$ concentration and incubation time.

As photoactive material, the mass ratio of $Ag_2S@WS_2$ can greatly influence the detection sensitivity. Thus it was investigated firstly. As shown in Fig. 5A, the photocurrent gradually increased with changing the mass ratio from 10% to 15%. Then, the photocurrent decreased when further increasing the mass ratio. Therefore, a 15% mass ratio was chosen for subsequent experiments. Expect mass ratio, the concentration of $Ag_2S@WS_2$ can also influence the PEC response of the biosensor (Fig. 5B). The photocurrent enlarged with varying the concentration of $Ag_2S@WS_2$ from 0.5 to 2 mg/mL. However, when the concentration increased further, the photocurrent decreased. It is attributed to the increased thickness of $Ag_2S@WS_2$, which hinders the transfer of electrons to the electrode surface and increases the recombination of photoelectrons with holes. Thus, 2 mg/mL $Ag_2S@WS_2$ was selected for subsequent experiments.

As for a kind of 5fdCTP capture reagent, the amount of Au@AHMT will greatly influence the detection sensitivity. To optimize Au@AHMT concentration, different amount of Au@AHMT was modified. As illustrated in Fig. 5C, the photocurrent showed a tendency to decrease firstly and then to stabilize with increasing the concentration of Au@AHMT. It was ascribed to the increased amount of Au@AHMT on electrode surface, which caused the decreased photocurrent. However, when further increasing Au@AHMT concentration, the amount of Au@AHMT was saturated, which did not lead the increased immobilization amount of 5fdCTP and $FeVO_4$. Therefore, 2 mg/mL Au@AHMT was used.

As detection target, 5fdCTP capture efficiency is crucial. Thus, the

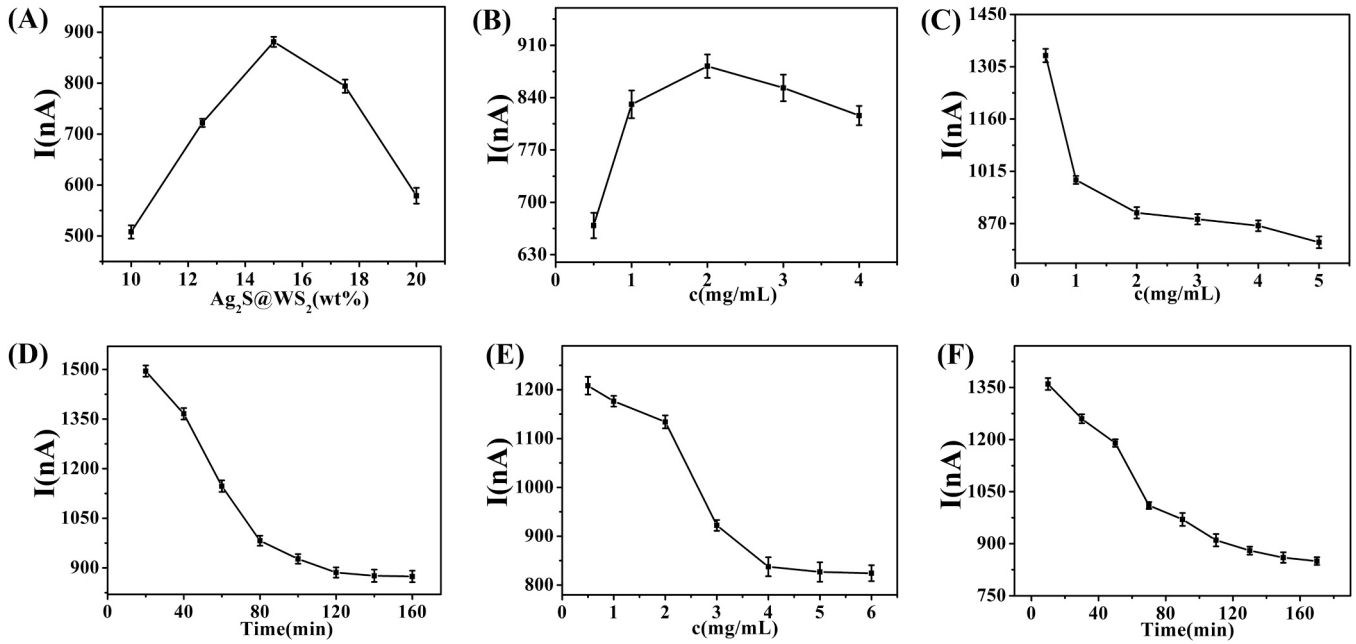

Fig. 5. Effect of mass ratios of WS_2 and Ag_2S (A), concentration of $Ag_2S@WS_2$ (B) and Au@AHMT (C), 5fdCTP incubation time (D), $FeVO_4$ concentration (E) and incubation time (F) on the PEC response of the biosensor.

incubation time of 5fdCTP was optimized. As shown in Fig. 5D, the photocurrent reduced with extending incubation time from 10 to 120 min. Then, the photocurrent became stable with further prolonging the incubation time, which was attributed to the saturated immobilization of 5fdCTP. Thus, 120 min was employed.

$FeVO_4$ was employed as nanozyme to catalyze the oxidation of 4-chloro1-naphthol to produce benzene-4-chlorohexanedione, causing decreased PEC response. Thus, the immobilization amount of $FeVO_4$ can greatly influence the PEC response. Thus, the immobilization time and concentration of $FeVO_4$ were optimized. The results were listed in Fig. 5E and F. The photocurrent reduced with enlarging $FeVO_4$ concentration from 0.5 to 4 mg/mL. However, the photocurrent did not change obviously with further improving $FeVO_4$ concentration. It was caused by the saturated immobilization of $FeVO_4$ on electrode surface. Therefore, 4 mg/mL $FeVO_4$ was selected. Fig. 5F showed the influence of the incubation time of $FeVO_4$. The results indicated that 130 min was employed in this work.

Table 1
Performance comparison of the PEC biosensor with other methods for 5fC detection.

Methods	Linear range	Detection limit	Reaction time	Ref
Fluorescence	50–1000 nM	42 nM	More than 24 h	(Guo et al., 2013)
Fluorescence	5–200 nM	10 nM	More than 24 h	(Xu et al., 2014)
SPME-UPLC-ESI-MS/MS	0.1–100 fM	0.03 fM	About 22 h	(Jiang et al., 2017)
LC-ESI-MS/MS	0.5–100 fM	0.11 fM	About 12 h~27 h	(Tang et al., 2015)
Photoelectrochemistry	0.1–400 nM	0.03 nM	About 5 h	This work

3.6. Performance of the biosensor for 5fdCTP detection

To assess the detection sensitivity of the developed method, the PEC response of the biosensor with different concentrations of 5fdCTP was investigated. Under optimal experimental conditions, the photocurrent of the biosensor decreased with changing 5fdCTP concentration from 0.1 to 400 nM (Fig. 6A). As presented in Fig. 6B, the photocurrent of the biosensor showed linear relationship with the logarithm value of 5fdCTP concentration. The detection limit was 0.062 nM (3σ). The detection performances of this method were compared with other work and the results were listed in Table 1. Although the detection limit of this method is higher than LC-MS technique, our work possesses the merits of fast response, simple operation, inexpensive instrument.

Detection selectivity is a key property affecting the detection performance of biosensor. Therefore, it was assessed. To perform it, different nucleotides were employed as possible interfering substances, which coexisted with 5fC in the genomic DNA, including 5mdCTP, 5hmdCTP and m^6dATP. The biosensor was fabricated as described in section 2.6 except that different nucleotide was employed. Then, the photocurrent variety ($\Delta I = I_b - I_a$) was compared, where I_b was the photocurrent of Au@AHMT/Ag_2S@WS_2/ITO, and I_a was the photocurrent of Au@AHMT/Ag_2S@WS_2/ITO after incubated successively with nucleotides and $FeVO_4$. As shown in Fig. 6C, the ΔI for 5fdCTP was highest, indicating good specificity of the developed method. To further testify the good selectivity of this method, the mixture solution of 5fdCTP and other nucleotides was employed as detection targets. The photocurrent of the biosensor fabricated with the mixture solution was similar with the biosensor fabricate with 5fdCTP, which further verified the good specificity.

The reproducibility is another pivotal parameter for analytical method. To assess it, seven of $FeVO_4$/5fC/Au@AHMT/Ag_2S@WS_2/ITO electrodes were prepared using 10 nM 5fdCTP and the photocurrent was

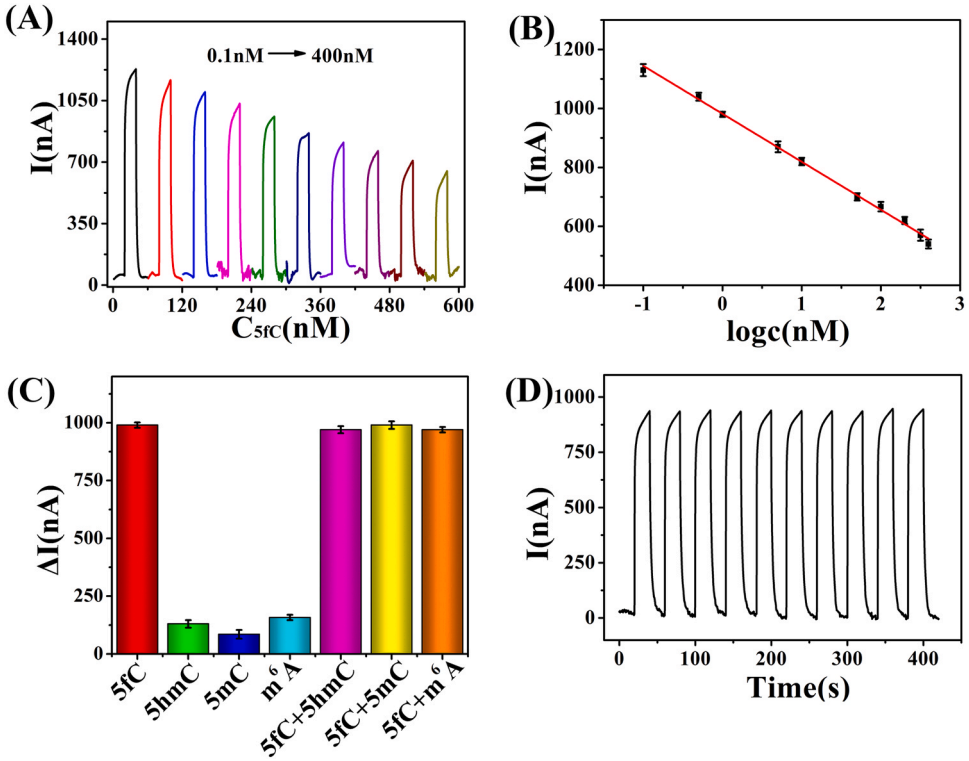

Fig. 6. (A) The PEC response of the biosensor with different concentrations of 5fdCTP. (a–j) 0.1, 0.5, 1, 5, 10, 50, 100, 200, 300, 400 nM. (B) Calibration curve. (C) The histogram of photocurrent changes of the biosensor fabricated with different targets. (D) Time-based photocurrent response of the biosensor with light on and off.

recorded. The RSD of the PEC response was 3.5% (Fig. S3), implying acceptable reproducibility.

Stability is another important property for biosensors. The photocurrent of the sensor was detected for more than 10 consecutive cycles. In cyclic testing, the photocurrent response of the PEC sensor was detected for 10 consecutive cycles with little variation and a stable peak shape. The RSD of the PEC response was 1.42% (Fig. 6D), indicating the good stability.

3.7. Detection of 5fC in samples

With the rapid development of agriculture and industry, the pollution of water and soil by heavy metals is becoming increasingly serious. Heavy metals enter into the water and soil through various pathways to cause heavy metal pollution, producing toxic effects on crops and causing the reduction of crop yield and quality. More seriously, heavy metal can even enter into the food chain, causing harm to human health (Li et al., 2012; Wei et al., 2008). Among various heavy metals, Hg and Cd are the typical heavy metal pollutants in the environment, which lead to metabolic disorder in the body, inhibit growth and development, and even lead to death (Guanxing et al., 2010; Salazar et al., 2012). Thus, to evaluate the applicability of the PEC biosensor, the influence of heavy metal on the content of 5fC in rice seedling tissues was investigated. To carry out this work, the samples were treated as introduced in section 2.7. The biosensor was fabricated as the process in section 2.6 except that 5fdCTP was replaced by the extracted nucleotides mixture from the leaves and roots of rice seedlings. Firstly, the apparent influence was firstly studied. As illustrated in Fig. 7A, with increasing Hg^{2+} concentration from 0.1 to 10 mg/L, the seedlings root shortened gradually accompanying the slowed growth of the plant. The similar phenomenon was also obtained with Cd^{2+} (Fig. 7D). To further understand the effect of heavy metal on 5fC content in the leaves and roots of rice seedlings, 5fC expression was investigated by PEC method. As shown in Fig. 7B,C and E,F, different influence was achieved with different heavy metals. For Hg^{2+}, it promoted the content of 5fC in genomic DNA of the leaves with increasing concentration (Fig. 7B). Similarly, Hg^{2+} also promoted 5fC content in genomic DNA of rice seedling roots (Fig. 7C). For Cd^{2+}, low concentration of Cd^{2+} greatly promoted 5fC content, while the promotion tendency of high concentration of Cd^{2+} decreased (Fig. 7E and F). These results indicated the complexity of the influence of heavy metal on 5fC content in genomic DNA of rice seedling tissues. Based on these investigation, 5fC might be as a new biomarker for the evaluation of the eco-toxicological effects of heavy metals towards rice.

As for serious heavy metal pollution, practical and feasible restoration techniques are essential. Biomass based hydrochar presents the merits of abundant raw material, high specific surface area, strong adsorption ability for heavy metal, low biotoxicity. More importantly, it can react with heavy metal ions by precipitation or chelate with some specific modified functional groups, which can change heavy metals from the active state to the residue state. In addition, hydrochar can also reduce the enrichment of heavy metals by adsorbing heavy metal ions in water, while reducing its biological effectiveness (Le et al., 2019). Thus hydrochar might be an ideal repair material for heavy metal pollution (Liu et al., 2020; Kazak and Tor, 2020; Yue et al., 2019). Thus, to further investigate the applicability, the influence of hydrochar on decreasing the biotoxicity of heavy metals was investigated. As described in section 2.7, heavy metal solution was firstly adsorbed by hydrochar, then the filtrate was used to cultrate the rice seedlings. Finally, 5fC in extracted genomic DNA was detected by PEC method. As shown in Fig. 8A and B, after hydrochar treatment, the apparent traits were improved greatly. When the rice seedlings were incubated with Hg^{2+} and Cd^{2+}, the rice seedlings developed slowly with short root and plant length compared with control sample (Fig. 8A). However, after treatment with hydrochar, the plant development was greatly improved (Fig. 8B), which should be ascribed to the adsorption ability of hydrochar to heavy metal, decreasing the concentration of heavy metal. To further understand the change of 5fC content, it was measured by PEC method. As illustrated in Fig. 8C and D, after incubated with 10 mg/L heavy metal, the expression of 5fC was all improved. However, when the pollution solution was treated with hydrochar, 5fC content was decreased with different extent. As for Cd^{2+}, the content of 5fC decreased to that as control, which indicated that almost all Cd^{2+} was adsorbed by hydrochar. However, as for Hg^{2+}, the expression of 5fC only reduced a little, causing by the weak adsorption ability of hydrochar to Hg^{2+}. According to these results, the influence of hydrochar on the biotoxicity of heavy metal is positive, which may be applied to repair heavy metal pollution in water.

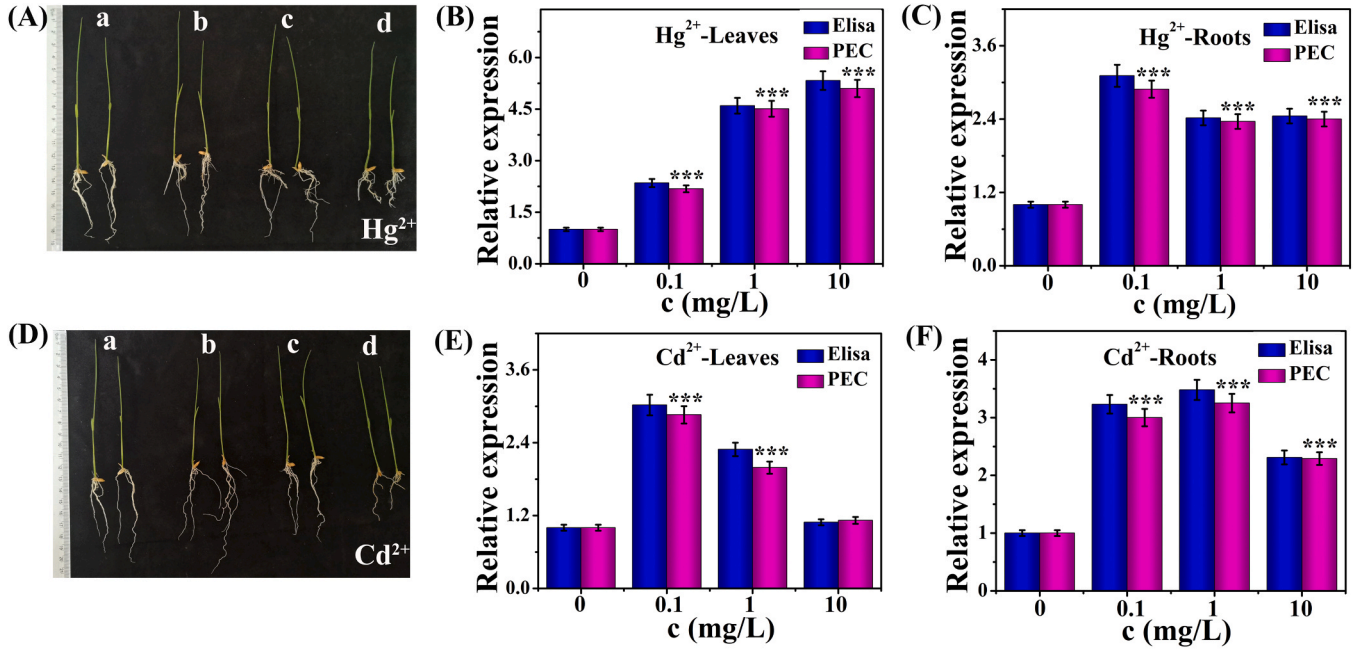

Fig. 7. Effects of heavy metals on the leaves and roots of rice seedlings (A and D). (A) Hg^{2+}, (D) Cd^{2+}. (a–d) 0, 0.1, 1, 10 mg/L. Effect of heavy metals on 5fC content in the genomic DNA of the leaves (B and E) and roots (C and F) of rice seedling. (Compared with the control group. NS, no significant, $p > 0.05$; *, $p < 0.05$; **, $p < 0.01$; ***, $p < 0.001$).

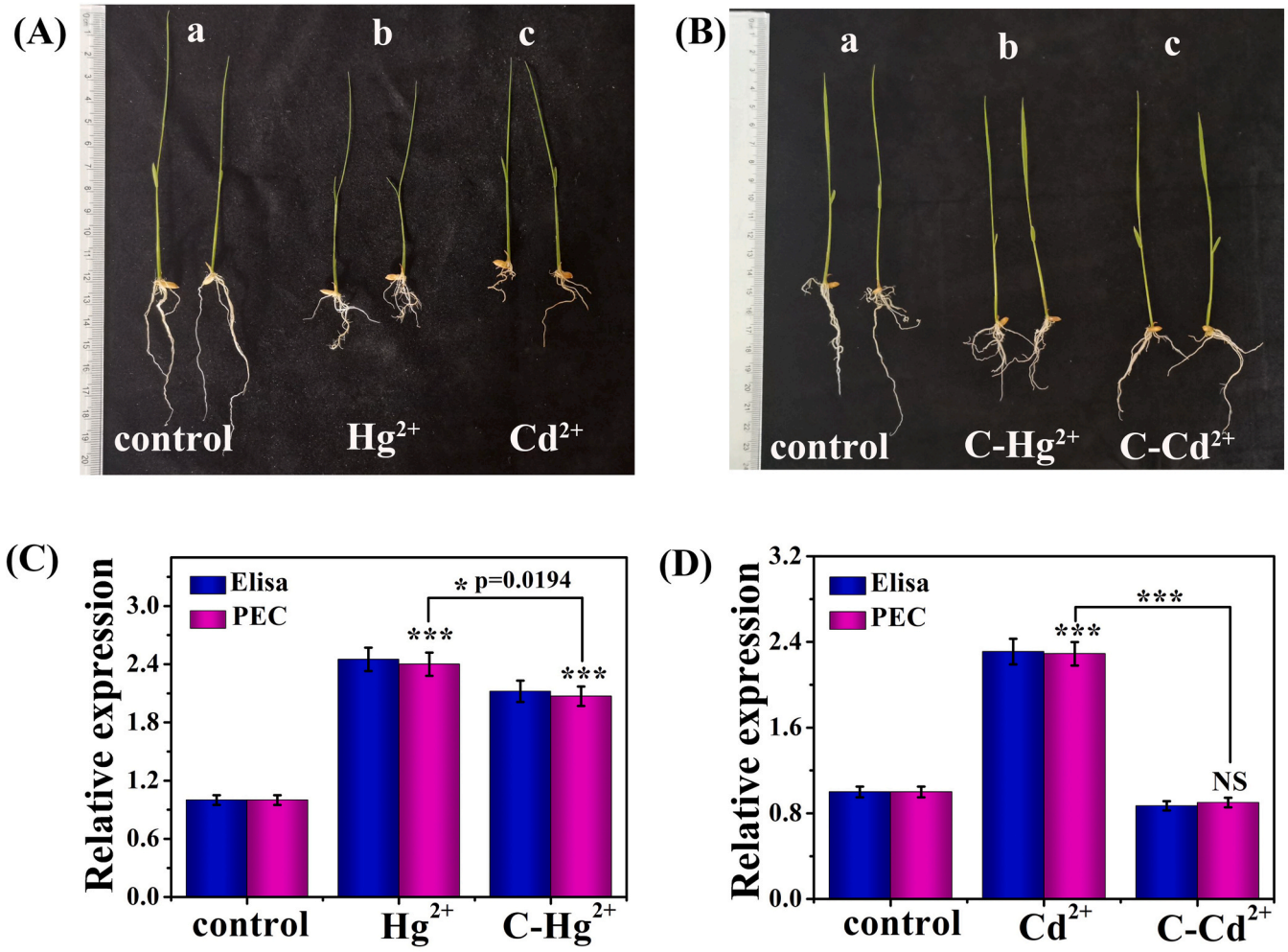

Fig. 8. (A) Photograph of rice seedlings after incubated with 10 mg/L heavy metals. (B) Photograph of rice seedlings after incubated with the filtrate of 10 mg/L heavy metals and 2 mg/L hydrochar (marked as C-Hg^{2+} and C-Cd^{2+}). (C and D) Effect of hydrochar on the toxicity of heavy metal towards rice seedlings. (Compared with the control group. NS, no significant, $p > 0.05$; *, $p < 0.05$; **, $p < 0.01$; ***, $p < 0.001$).

However, considering the relative weak adsorption of Hg^{2+}, the prepared hydrochar should be modified to improve the heavy metal adsorption performance.

4. Conclusions

In summary, the influence of hydrochar on the biotoxicity of heavy metal was investigated using 5fC as new biomarker and PEC technique as new evaluation method. Firstly, a simple and sensitive PEC detection platform was constructed using $Ag_2S@WS_2$ as photoactive material, Au@AHMT as 5fC recognition and capture reagent, and $FeVO_4$ as PEC response inhibitor. This method presented high detection sensitivity and selectivity for 5fC based on the effective signal amplification and covalent recognition of 5fC. Using 5fC as biomarker, the biotoxicity of Hg^{2+} and Cd^{2+} to rice was investigated with the increased content with different concentrations of heavy metal. In addition, the decreased biotoxicity of heavy metal by hydrochar were also proved. This work not only provides new and sensitive technique for 5fC detection, but also offers new biomarker and new evaluation method for eco-toxicological effects of heavy metals.

CRediT authorship contribution statement

Qian Wang: Data curation, Formal analysis, Funding acquisition, Investigation, Methodology, Validation, Project administration, Writing - review & editing. **Huanshun Yin**: Data curation, Formal analysis, Project administration, Validation, Supervision, Writing - review & editing. **Yunlei Zhou**: Data curation, Formal analysis, Investigation, Methodology. **Jun Wang**: Data curation, Project administration, Validation, Supervision, Writing - review & editing. **Shiyun Ai**: Project administration, Validation, Supervision.

Declaration of Competing Interest

The authors declare that they have no known competing financial interests or personal relationships that could have appeared to influence the work reported in this paper.

Acknowledgments

This work was supported by the National Key Research and Development Project of China (2018YFC1800605), Outstanding Youth Innovation Team of University in Shandong Province (2019KJC019), Key Research and Development Project of Shandong Province (2019GSF109026, 2019GSF107023), National Natural Science Foundation of China (Nos. 21775090, 41807484, 41977345, 42077363), Special Funds of Taishan Scholar of Shandong Province of China.

Appendix A. Supporting information

Supplementary data associated with this article can be found in the online version at doi:10.1016/j.jhazmat.2021.125293.

References

Ahmed Ouameur, H.A.A., Ahmad, R., Naoui, M., Tajmir-Riahi, H.A., 2005. A comparative study of Fe(II) and Fe(III) interactions with DNA duplex: major and minor grooves bindings. DNA Cell Biol. 24, 394–401.

Cai, G., Yu, Z., Ren, R., Tang, D., 2018. Exciton-plasmon interaction between AuNPs/Graphene nanohybrids and CdS quantum dots/TiO_2 for photoelectrochemical aptasensing of prostate-specific antigen. ACS Sens. 3, 632–639.

Cao, J.-T., Wang, B., Dong, Y.-X., Wang, Q., Ren, S.-W., Liu, Y.-M., Zhao, W.-W., 2018. Photogenerated hole-Induced chemical redox cycling on $Bi_2S_3/Bi_2Sn_2O_7$ heterojunction: toward general amplified split-type photoelectrochemical immunoassay. ACS Sens. 3, 1087–1092.

Chhowalla, M., Shin, H.S., Eda, G., Li, L.J., Loh, K.P., Zhang, H., 2013. The chemistry of two-dimensional layered transition metal dichalcogenide nanosheets. Nat. Chem. 5, 263–275.

Di, L., Yang, H., Xian, T., Liu, X., Chen, X., 2019. Photocatalytic and photo-fenton catalytic degradation activities of z-scheme $Ag_2S/BiFeO_3$ heterojunction composites under visible-light irradiation. Nanomaterials 9, 399.

Guanxing, H., Jichao, S., Yuxi, Z., Jihong, J., Jingtao, L., 2010. Distribution of lead in water and soil of representative area in pearl river delta. Res. Environ. Sci. 23, 137–143.

Guo, P., Yan, S., Hu, J., Xing, X., Wang, C., Xu, X., Qiu, X., Ma, W., Lu, C., Weng, X., Zhou, X., 2013. Selective detection of 5-formyl-2′-deoxycytidine in DNA using a fluorogenic hydroxylamine reagent. Org. Lett. 15, 3266–3269.

Hao, N., Hua, R., Chen, S., Zhang, Y., Zhou, Z., Qian, J., Liu, Q., Wang, K., 2017. Multiple signal-amplification via Ag and TiO_2 decorated 3D nitrogen doped graphene hydrogel for fabricating sensitive label-free photoelectrochemical thrombin aptasensor. Biosens. Bioelectron. 101, 14–20.

Hao, N., Hua, R., Zhang, K., Lu, J., Wang, K., 2018. A sunlight powered portable photoelectrochemical biosensor based on a potentiometric resolve ratiometric principle. Anal. Chem. 90, 13207–13211.

He, Q., Sun, H., Shang, Y., Tang, Y., She, P., Zeng, S., Xu, K., Lu, G., Liang, S., Yin, S., Liu, Z., 2018. Au@TiO2 yolk-shell nanostructures for enhanced performance in both photoelectric and photocatalytic solar conversion. Appl. Surf. Sci. 441, 458–465.

Jiang, H., Liu, T., Guo, N., Yu, L., Yuan, B., Feng, Y., 2017. Determination of formylated DNA and RNA by chemical labeling combined with mass spectrometry analysis. Anal. Chim. Acta 981, 1–10.

Kazak, O., Tor, A., 2020. In situ preparation of magnetic hydrochar by co-hydrothermal treatment of waste vinasse with red mud and its adsorption property for Pb(II) in aqueous solution. J. Hazard. Mater. 393, 122391.

Le, Yue, Fei, Lian, Yang, Han, Qiongli, Bao, Zhengyu, Wang, 2019. The effect of biochar nanoparticles on rice plant growth and the uptake of heavy metals: implications for agronomic benefits and potential risk. Sci. Total Environ. 656, 9–18.

Li, F., Wang, S., Yin, H., Chen, Y., Zhou, Y., Huang, J., Ai, S., 2020. Photoelectrochemical biosensor for DNA formylation detection in genomic DNA of maize seedlings based on black TiO_2-enhanced photoactivity of MoS_2/WS_2 heterojunction. ACS Sens. 5, 1092–1101.

Li, F., Zhou, Y., Yin, H., Ai, S., 2020. Recent advances on signal amplification strategies in photoelectrochemical sensing of microRNAs. Biosens. Bioelectron. 166, 112476.

Li, Q., Chen, Y., Fu, H., Cui, Z., Shi, L., Wang, L., Liu, Z., 2012. Health risk of heavy metals in food crops grown on reclaimed tidal flat soil in the pearl river estuary, China. J. Hazard. Mater. 227, 148–154.

Li, X., Zhu, L., Zhou, Y., Yin, H., Ai, S., 2017. Enhanced photoelectrochemical method for sensitive detection of protein kinase a activity using TiO_2/g-C_3N_4, PAMAM dendrimer, and alkaline ahosphatase. Anal. Chem. 89, 2369–2376.

Li, X., Xiong, J., Gao, X., Ma, J., Huang, J., 2020. Novel BP/BiOBr S-scheme nano-heterojunction for enhanced visible-light photocatalytic tetracycline removal and oxygen evolution activity. J. Hazard. Mater. 387, 121690.

Lin, Y., Han, D., Li, Y., Tan, L., Liu, X., Cui, Z., Yang, X., Li, Z., Liang, Y., Zhu, S., Wu, S., 2019. $Ag_2S@WS_2$ heterostructure for rapid bacteria-killing using near-infrared light. ACS Sustain. Chem. Eng. 7, 14982–14990.

Liu, C., Wang, Y., Yang, W., Wu, F., Zeng, W., Chen, Z., Huang, J., Zou, G., Zhang, X., Wang, S., Weng, X., Wu, Z., Zhou, Y., Zhou, X., 2017. Fluorogenic labeling and single-base resolution analysis of 5-formylcytosine in DNA. Chem. Sci. 8, 7443–7447.

Liu, X., Zhai, Y., Li, S., Wang, B., Wang, T., Liu, Y., Qiu, Z., Li, C., 2020. Hydrothermal carbonization of sewage sludge: effect of feed-water pH on hydrochar's physicochemical properties, organic component and thermal behavior. J. Hazard. Mater. 388, 122084.

Lopez, V., Fernandez, A.F., Fraga, M.F., 2017. The role of 5-hydroxymethylcytosine in development, aging and age-related diseases. Ageing Res. Rev. 37, 28–38.

Muche, M.S., Göbel, M.W., 1996. Bis(guanidinium) alcohols as models of staphylococcal nuclease: substrate binding through Ion pair complexes and fast phosphoryl transfer reactions. Angew. Chem. Int. Ed. 35, 2126–2129.

Patolsky, F., Lichtenstein, A., Willner, I., 2003. Highly sensitive amplified electronic detection of DNA by biocatalyzed precipitation of an insoluble product onto electrodes. Chem. Eur. J. 9, 1137–1145.

Pfaffeneder, T., Hackner, B., Truß, M., Münzel, M., Müller, M., Deiml, C.A., Hagemeier, C., Carell, T., 2011. The discovery of 5-formylcytosine in embryonic stem cell DNA. Angew. Chem. 123, 7146–7150.

Pfaffeneder, T., Hackner, B., Trus, M., Munzel, M., Muller, M., Deiml, C., Hagemeier, C., Carell, T., 2011. The discovery of 5–formylcytosine in embryonic stem cell DNA. Angew. Chem. 50, 7008–7012.

Pumera, M., Loo, A.H., 2014. Layered transition-metal dichalcogenides (MoS_2 and WS_2) for sensing and biosensing. TrAC Trend Anal. Chem. 61, 49–53.

Reddy, D.A., Park, H., Ma, R., Kumar, D.P., Lim, M., Kim, T.K., 2017. Heterostructured WS_2-MoS_2 ultrathin nanosheets integrated on CdS nanorods to promote charge separation and migration and improve solar-driven photocatalytic hydrogen evolution. ChemSusChem 10, 1563–1570.

Ren, X., Qiao, H., Huang, Z., Tang, P., Liu, S., Luo, S., Yao, H., Qi, X., Zhong, J., 2018. Investigating the photocurrent generation and optoelectronic responsivity of WS_2-TiO_2 heterostructure. Opt. Commun. 406, 118–123.

Salazar, M.J., Rodriguez, J.H., Nieto, G.L., Pignata, M.L., 2012. Effects of heavy metal concentrations (Cd, Zn and Pb) in agricultural soils near different emission sources on quality, accumulation and food safety in soybean [Glycine max (L.) Merrill]. J. Hazard. Mater. 233, 244–253.

Shi, X.M., Mei, L.P., Wang, Q., Zhao, W.W., Xu, J.J., Chen, H.Y., 2018. Energy transfer between semiconducting polymer dots and gold nanoparticles in a photoelectrochemical system: a case application for cathodic bioanalysis. Anal. Chem. 90, 4277–4281.

Shu, J., Qiu, Z., Lin, Z., Cai, G., Yang, H., Tang, D., 2016. Semiautomated support photoelectrochemical immunosensing platform for portable and high-throughput immunoassay based on Au nanocrystal decorated specific crystal facets $BiVO_4$ photoanode. Anal. Chem. 88, 12539–12546.

Tan, C., Cao, X., Wu, X.J., He, Q., Yang, J., Zhang, X., Chen, J., Zhao, W., Han, S., Nam, G.H., 2017. Recent advances in ultrathin two-dimensional nanomaterials. Chem. Rev. 117, 6225–6331.

Tang, Y., Zheng, S.J., Qi, C.B., Feng, Y.Q., Yuan, B.F., 2015. Sensitive and simultaneous determination of 5-methylcytosine and its oxidation products in genomic DNA by chemical derivatization coupled with liquid chromatography-tandem mass spectrometry analysis. Anal. Chem. 87, 3445–3452.

Vega-Mayoral, V., Backes, C., Hanlon, D., Khan, U., Gholamvand, Z., O'Brien, M., Duesberg, G.S., Gadermaier, C., Coleman, J.N., 2016. Photoluminescence from liquid-exfoliated WS_2 Monomers in poly(vinyl alcohol) polymer composites. Adv. Funct. Mater. 26, 1028–1039.

Wang, H., Zhu, L., Duan, J., Wang, M., Yin, H., Wang, P., Ai, S., 2018. Photoelectrochemical biosensor for HEN1 RNA methyltransferase detection using peroxidase mimics PtCu NFs and poly(U) polymerase-mediated RNA extension. Biosens. Bioelectron. 103, 32–38.

Wang, H., Yin, H., Huang, H., Li, K., Zhou, Y., Waterhouse, G.I.N., Lin, H., Ai, S., 2018. Dual-signal amplified photoelectrochemical biosensor for detection of N6-methyladenosine based on $BiVO_4$-110-TiO_2 heterojunction, Ag^+-mediated cytosine pairs. Biosens. Bioelectron. 108, 89–96.

Wang, M., Yin, H., Zhou, Y., Sui, C., Wang, Y., Meng, X., Waterhouse, G.I.N., Ai, S., 2019. Photoelectrochemical biosensor for microRNA detection based on a MoS_2/g-C_3N_4/black TiO_2 heterojunction with histostar@AuNPs for signal amplification. Biosens. Bioelectron. 128, 137–143.

Wang, S., Long, Y., Wang, J., Ge, Y., Guo, P., Liu, Y., Tian, T., Zhou, X., 2013. Systematic investigations of different cytosine modifications on CpG dinucleotide sequences: the effects on the B-Z transition. J. Am. Chem. Soc. 136, 56–59.

Wang, Y., Zhou, C., Wang, W., Zhao, Y., 2013. Preparation of two dimensional atomic crystals BN, WS_2, and MoS_2 by supercritical CO_2 assisted with ultrasound. Ind. Eng. Chem. Res. 52, 4379–4382.

Wei, R.B., Huang, Z.L., Gu, G.H., Wang, Z., Zeng, L., Chen, Y., Liu, Z.Q., 2018. Dual-cocatalysts decorated rimous CdS spheres advancing highly-efficient visible-light photocatalytic hydrogen production. Appl. Catal. B Environ. 231, 101–107. S0926337318302042.

Wei, S., Silva, J.A.T.D., Zhou, Q., 2008. Agro-improving method of phytoextracting heavy metal contaminated soil. J. Hazard. Mater. 150, 662–668.

Wilson, J.A., Yoffe, A.D., 1969. The transition metal dichalcogenides discussion and interpretation of the observed optical, electrical and structural properties. Adv. Phys. 18, 193–335.

Xu, L., Chen, Y., Chong, J., Fin, A., Mccoy, L.S., Xu, J., Zhang, C., Wang, D., 2014. Pyrene-based quantitative detection of the 5–formylcytosine loci symmetry in the CpG duplex content during TET-dependent demethylation. Angew. Chem. 53, 11223–11227.

Xu, L., Duan, W., Chen, F., Zhang, J., Li, H., 2020. A photoelectrochemical aptasensor for the determination of bisphenol a based on the Cu (I) modified graphitic carbon nitride. J. Hazard. Mater. 400, 123162.

Xu, Z., Zhang, Y., Lin, S., Zheng, C., Zhong, Y.L.L., Xia, X., Li, Z., Sophia, P.J., Fuhrer, M. S., Cheng, Y., 2015. Synthesis and transfer of large-area monolayer WS_2 crystals: moving toward the recyclable use of sapphire substrates. ACS Nano 9, 6178–6187.

You, F., Wei, J., Cheng, Y., Wen, Z., Wang, K., 2020. A sensitive and stable visible-light-driven photoelectrochemical aptasensor for determination of oxytetracycline in tomato samples. J. Hazard. Mater. 398, 122944.

Yu, Y., Ju, P., Zhang, D., Han, X., Yin, X., Zheng, L., Sun, C., 2016. Peroxidase-like activity of $FeVO_4$ nanobelts and its analytical application for optical detection of hydrogen peroxide. Sens. Actuators B Chem. 233, 162–172.

Yuan, Y., Li, R., Liu, Z., 2014. Establishing water-soluble layered WS_2 nanosheet as a platform for biosensing. Anal. Chem. 86, 3610–3615.

Yuan, Y., Hu, T., Zhong, X., Zhu, M., Chai, Y., Yuan, R., 2020. Highly sensitive photoelectrochemical biosensor based on quantum dots sensitizing Bi2Te3

nanosheets and DNA-amplifying strategies. ACS Appl. Mater. Interfaces 12, 22624–22629.
Yue, L., Lian, F., Han, Y., Bao, Q., Wang, Z., Xing, B., 2019. The effect of biochar nanoparticles on rice plant growth and the uptake of heavy metals: implications for agronomic benefits and potential risk. Sci. Total Environ. 656, 9–18.
Zang, Y., Ju, Y., Hu, X., Zhou, H., Yang, Z., Jiang, J., Xue, H., 2018. WS_2 nanosheets-sensitized CdS quantum dots heterostructure for photoelectrochemical immunoassay of alpha-fetoprotein coupled with enzyme-mediated biocatalytic precipitation. Analyst 143, 2895–2900.
Zhang, K., Lv, S., Lin, Z., Li, M., Tang, D., 2018. Bio-bar-code-based photoelectrochemical immunoassay for sensitive detection of prostate-specific antigen using rolling circle amplification and enzymatic biocatalytic precipitation. Biosens. Bioelectron. 101, 159–166.
Zhang, L., Shi, X.M., Xu, Y.T., Fan, G.C., Yu, X.D., Liang, Y.Y., Zhao, W.W., 2019. Binding-induced formation of DNAzyme on an Au@Ag nanoparticles/TiO_2 nanorods electrode: stimulating biocatalytic precipitation amplification for plasmonic photoelectrochemical bioanalysis. Biosens. Bioelectron. 134, 103–108.
Zhao, W.W., Ma, Z.Y., Yu, P.P., Dong, X.Y., Xu, J.J., Chen, H.Y., 2012. Highly sensitive photoelectrochemical immunoassay with enhanced amplification using horseradish peroxidase induced biocatalytic precipitation on a CdS quantum dots multilayer electrode. Anal. Chem. 84, 917–923.
Zhao, W.W., Xu, J.J., Chen, H.Y., 2018. Photoelectrochemical immunoassays. Anal. Chem. 90, 615–627.
Zhao, X., Ma, X., Sun, J., Li, D., Yang, X., 2016. Enhanced catalytic activities of surfactant-assisted exfoliated WS_2 nanodots for hydrogen evolution. ACS Nano 10, 2159–2166.
Zhou, Y., Yin, H., Zhao, W.W., Ai, S., 2020. Electrochemical, electrochemiluminescent and photoelectrochemical bioanalysis of epigenetic modifiers: a comprehensive review. Coord. Chem. Rev. 424, 213519.